OPEN ACCESS
IOP Publishing
Journal of Optics
J. Opt. **26** (2024) 075001 (9pp)
https://doi.org/10.1088/2040-8986/ad4722

Adaptive multi-spectral mimicking with 2D-material nanoresonator networks

Yujie Luo[1], Thomas Christensen[2] and Ognjen Ilic[1,*]

[1] Department of Mechanical Engineering, University of Minnesota, Minneapolis, MN 55455, United States of America
[2] Department of Electrical and Photonics Engineering, Technical University of Denmark, 2800 Kgs. Lyngby, Denmark

E-mail: ilic@umn.edu

Received 4 January 2024, revised 7 April 2024
Accepted for publication 3 May 2024
Published 17 May 2024

Abstract

Active nanophotonic materials that can emulate and adapt between many different spectral profiles—with high fidelity and over a broad bandwidth—could have a far-reaching impact, but are challenging to design due to a high-dimensional and complex design space. Here, we show that a metamaterial network of coupled 2D-material nanoresonators in graphene can adaptively match multiple complex absorption spectra via a set of input voltages. To design such networks, we develop a semi-analytical auto-differentiable dipole-coupled model that allows scalable optimization of high-dimensional networks with many elements and voltage signals. As a demonstration of multi-spectral capability, we design a single network capable of mimicking four spectral targets resembling select gases (nitric oxide, nitrogen dioxide, methane, nitrous oxide) with very high fidelity ($>90\%$). Our results could impact the design of highly reconfigurable optical materials and platforms for applications in sensing, communication and display technology, and signature and thermal management.

Supplementary material for this article is available online

Keywords: metamaterials, 2D materials, tunable optics

1. Introduction

The principles of metamaterial optics have made it possible to realize complex spectral responses that are not found in conventional materials. The burgeoning field of optical metamaterials, including artificial structures like dielectric metalenses, photonic crystal thermal emitters, or signal-processing metasurfaces, has inspired numerous applications across optical and photonic technologies [1–6]. For the most part, such structures are static. They are often designed to have a target spectral response and, once fabricated, their properties cannot be changed. Going beyond such single-spectrum metamaterials, a broader set of questions emerges: to what extent can a single device or structure replicate ('mimic') and reconfigure between a range of complex spectral targets? What are the optical design principles to make such structures, and, are these principles specific to given targets or can they be made universal?

Active and reconfigurable optical platforms—structures and devices whose optical behavior can be dynamically tuned—could play a pivotal role in a broad range of applications [7–14], but designing a single structure that can accurately emulate many different spectra poses a complex design challenge. The root of the complexity lies in a parameter space that is inherently high dimensional. For a reconfigurable metamaterial or metasurface, the combination of a continuum of allowable geometrical parameters (i.e.

* Author to whom any correspondence should be addressed.

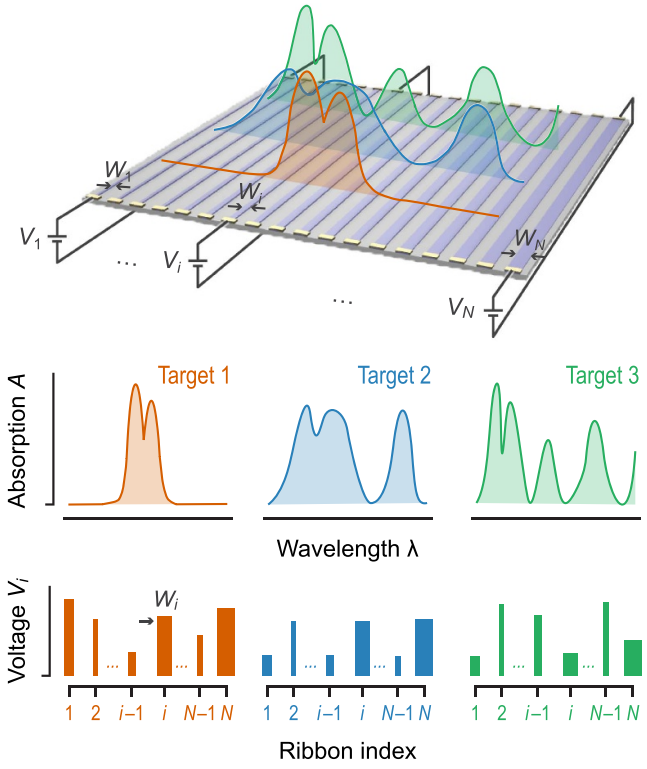

Figure 1. Multi-spectral photonic reconfigurability. A network of coupled elements in a single device adaptively mimics multiple complex spectral targets under a controlled external input. For a network of nano-structured graphene ribbons of optimized sizes W_i, applied voltage profiles V_i switch between multiple absorptivity spectra indicated by Targets 1 (orange), 2 (blue), and 3 (green).

nano-structure shape, size, and dimensionality) and material properties (i.e. refractive index) make the design space large and extracting intuition difficult. The unit cell can assume a range of topologies and symmetries in one, two, or three dimensions, and optical properties can be tuned in various ways, such as by mechanical deformation [15–17], electrostatic and electrochemical effects [18–21], and material phase changes [22–27]. Presently, designing active devices with multi-spectral capabilities in such a complex parameter space is often conceptually challenging and computationally demanding.

Here, we analyze the multi-spectral capability of a 2D-material nanoresonator network in graphene to adapt between a range of spectral targets. As shown in figure 1, the network consists of optically coupled nanoribbons whose response depends on parameters set during fabrication (such as element size and arrangement in the network) and parameters that can be tuned post-fabrication (such as voltage). Graphene, being a 2D semi-metal, has optical properties that can be strongly influenced by electric fields, leading to its use in tunable applications such as electronic modulation of emission [28–31] infrared absorption [32, 33], tunable scattering [34, 35], and amplitude and phase modulation [36–38], among others.

The goal of this work is to explore the potential of a single graphene network to reconfigure between multiple complex spectral targets, such as those found in the spectral absorption features of select gases. Absorption spectra of gases represent useful spectral targets since they are characterized by both narrow resonances and broader spectral envelopes.

We approach the problem of reconfigurable spectral mimicking in several steps: first, we develop and validate a semi-analytical dipole-coupled model that is numerically efficient; second, we implement the model to make it compatible with modern auto-differentiation techniques, ensuring efficient optimization of high-dimensional networks with many elements. We consider a network of nanoribbons because it provides an experimentally relevant platform with multiple input ports for mimicking and tuning between different spectra, and because it can be accurately described by a semi-analytical model. Next, we use this approach to design a network that can mimic a spectrum resembling nitric oxide (NO) with high fidelity, in both a planar and a stratified configuration. Finally, we demonstrate multi-spectral reconfigurability by designing a single network that can reconfigure between complex spectra resembling four gases.

2. Methods

Nanostructured plasmonic 2D elements, such as individual graphene ribbons, exhibit a resonant modal response that is governed by the element's size (ribbon width, W) and material response (conductivity, σ) that is captured by a 2D polarizability [39, 40]:

$$\alpha(\omega) = 2W^3 \sum_n \frac{A_n}{\zeta_n - \zeta(\omega)}, \tag{1}$$

where A_n are dimensionless mode- and polarization-dependent oscillator amplitudes, ζ_n are dimensionless mode-dependent eigenvalues, and $\zeta(\omega) = 2\mathrm{i}\varepsilon_0\varepsilon_\mathrm{B}\omega W/\sigma(\omega)$ captures the frequency (ω), size (W), and response (σ) dependence (with vacuum ε_0 and relative background permittivities ε_B). The coefficients A_n and ζ_n depend solely on shape—but not the size or material—of the nanostructured element. For a ribbon, the quantum numbers n implicitly include the momentum along the ribbon: for normal incidence, we consider the zero-momentum limit where the dipole resonance is characterized by $\zeta_1 \approx 2.3159$ and $A_1 \approx 0.8791$. In total, we include the first 'bright' 6 ribbon modes, using the tabulated values of ζ_n and A_n from [40]. Graphene's conductivity is a sum of intra- and interband contributions, i.e. $\sigma(\omega) = \sigma_\mathrm{intra}(\omega) + \sigma_\mathrm{inter}(\omega)$, contributing spectral features of Drude- and Landau-damping kinds, respectively[3].

$$\sigma_\mathrm{intra}(\omega) = \frac{2\mathrm{i}e^2 k_\mathrm{B} T}{\pi\hbar^2(\omega + \mathrm{i}\gamma)} \ln\left[2\cosh\left(\frac{E_\mathrm{F}}{2k_\mathrm{B}T}\right)\right], \tag{2}$$

[3] The conductivity expression of equation (3) neglects the temperature-dependence of the interband term because the usual expressions for the temperature-dependence of the interband term [41, 42] are incompatible with the auto-differentation tools used here. This omission, however, has negligible impact on the overall response of the network due to the weakness of the temperature-dependence.

$$\sigma_{\text{inter}}(\omega) = \frac{\mathrm{i}e^2}{4\pi\hbar} \ln\left[\frac{2|E_{\text{F}}| - \hbar(\omega + \mathrm{i}\gamma)}{2|E_{\text{F}}| + \hbar(\omega + \mathrm{i}\gamma)}\right], \tag{3}$$

where k_{B} denotes the Boltzmann constant, e the electronic charge, $\hbar$ the reduced Planck's constant, γ a relaxation rate, and T the ambient temperature.

To model a network of nanoresonators, we consider coupling of multiple elements via their induced dipole moments, following the coupled dipole approach which captures the leading-order inter-element coupling. In particular, we consider a collection of $i = 1, \ldots, N$ ribbons, each of size W_i, Fermi energy $E_{\text{F}i}$, and associated polarizability α_i. For definiteness, we assume each ribbon to be of finite width along x, infinitely extended along y, infinitesimal along z, and define $\mathbf{r}_\perp \equiv (x, z)$ to denote the non-invariant coordinates. The induced dipole moment p_i of the i-th ribbon is proportional to the electric field *not* originating from the i-th ribbon itself, such that:

$$p_i = \varepsilon_0 \varepsilon_{\text{B}} \alpha_i(\omega) E_i', \tag{4}$$

where E_i' denotes the ribbon-averaged sum of the in-plane components of any external field, E_0, and the in-plane components of the induced fields of all other ribbons $E_{j\neq i}$:

$$E_i' \equiv \frac{1}{W_i}\int_i E_0(\mathbf{r}_\perp)\,\mathrm{d}x + \frac{1}{W_i}\int_i \sum_{j\neq i} E_j(\mathbf{r}_\perp)\,\mathrm{d}x, \tag{5}$$

with $\int_i \mathrm{d}x$ denoting integration over the i-th ribbon's in-plane extent. In turn, the dipole p_i induces a field $E_i(\mathbf{r}_\perp)$ originating from the i-th ribbon, whose in-plane components are

$$E_i(\mathbf{r}_\perp) = \omega^2 \mu_0 G(\mathbf{r}_\perp, \mathbf{r}_{\perp i}) p_i, \tag{6}$$

with $G(\mathbf{r}_\perp, \mathbf{r}_{\perp i})$ denoting the y-integrated xx-component of the nonretarded free-space Green function and $\mathbf{r}_{\perp i}$ the center coordinate of the i-th ribbon. Combining equations (4)–(6), we obtain a system of coupled equations, which we cast as:

$$\left(\mathbf{1} - k_{\text{B}}^2 \boldsymbol{\alpha}\mathbf{G}\right)\mathbf{p} = \varepsilon_0 \varepsilon_{\text{B}} \boldsymbol{\alpha} \mathbf{E}_0, \tag{7}$$

with wave number $k_{\text{B}}^2 \equiv \varepsilon_{\text{B}}\omega^2/c^2$, dipole moments $\mathbf{p} \equiv [p_1, \ldots, p_N]$, ribbon-averaged external fields $\mathbf{E}_0 \equiv \left[W_1^{-1}\int_1 E_0(\mathbf{r}_\perp)\,\mathrm{d}x, \ldots, W_N^{-1}\int_N E_0(\mathbf{r}_\perp)\,\mathrm{d}x\right]$, diagonal 'bare' polarizability matrix $\boldsymbol{\alpha} \equiv \mathrm{diag}(\alpha_1, \ldots, \alpha_N)$, and Green function matrix $(\mathbf{G})_{ij} \equiv (1 - \delta_{ij})\bar{G}_{ij}$ whose elements give the dipole-coupling between the i-th and j-th ribbon appendix A:

$$\begin{aligned}\bar{G}_{ij} &\equiv \frac{1}{W_i}\int_i G(\mathbf{r}_\perp, \mathbf{r}_{\perp j})\,\mathrm{d}x \\ &= \frac{2}{\pi k_{\text{B}}^2} \frac{4(x_{ij}^2 - z_{ij}^2) - W_i^2}{\left[(W_i + 2x_{ij})^2 + 4z_{ij}^2\right]\left[(W_i - 2x_{ij})^2 + 4z_{ij}^2\right]},\end{aligned} \tag{8}$$

where $x_{ij} \equiv x_i - x_j$ and $z_{ij} \equiv z_i - z_j$ are the center-to-center x- and z-separations, respectively, between the i-th and j-th ribbon.

It is convenient to express the solution to equation (7) in terms of a 'dressed' or effective polarizability $\boldsymbol{\alpha}_{\text{eff}} \equiv (\mathbf{1} - k_{\text{B}}^2 \boldsymbol{\alpha}\mathbf{G})^{-1}\boldsymbol{\alpha}$ such that the induced dipole amplitudes and ribbon-averaged total fields are $\mathbf{p} = \varepsilon_0\varepsilon_{\text{B}}\boldsymbol{\alpha}_{\text{eff}}\mathbf{E}_0$ and $\mathbf{E}' = (\mathbf{1} + k_{\text{B}}^2 \mathbf{G}\boldsymbol{\alpha}_{\text{eff}})\mathbf{E}_0$. Similarly, we can express the main quantity of interest in our present case—the total absorption P_{abs} due to a monochromatic and uniform external field—in terms of $\boldsymbol{\alpha}_{\text{eff}}$ and $\mathbf{G}$, cf:

$$\begin{aligned}P_{\text{abs}} &= \tfrac{1}{2}\mathrm{Re}\int \mathbf{J}^*(\mathbf{r}_\perp)\cdot\mathbf{E}(\mathbf{r}_\perp)\,\mathrm{d}V = -\tfrac{1}{2}\omega\,\mathrm{Im}\left(\mathbf{p}^\dagger\mathbf{E}'\right) \\ &= -\tfrac{1}{2}\varepsilon_0\varepsilon_{\text{B}}\omega\,\mathrm{Im}\left[(\boldsymbol{\alpha}_{\text{eff}}\mathbf{E}_0)^\dagger\left(\mathbf{1} + k_{\text{B}}^2\mathbf{G}\boldsymbol{\alpha}_{\text{eff}}\right)\mathbf{E}_0\right],\end{aligned} \tag{9}$$

where we have used that the induced current $\mathbf{J}(\mathbf{r}_\perp)$ is a sum over dipole terms $\mathrm{i}\omega p_i \hat{\mathbf{x}}$.

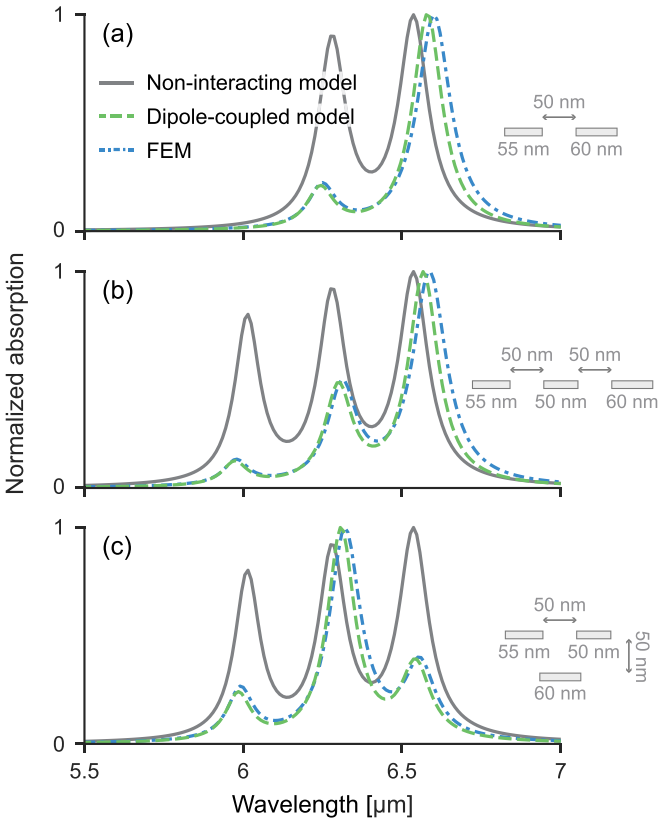

Figure 2. Validation of the network model. (a) two dissimilar elements in a planar configuration. (b) three dissimilar elements in a planar configuration. (c) three dissimilar elements in a stratified two-layer configuration. The dipole-coupled model (dashed green) matches well with finite-element simulations (FEM) in COMSOL (dashed-dotted blue). In contrast, a simple, non-interacting analysis that ignores inter-ribbon coupling (solid gray) models the response inadequately.

Figure 2 shows the implementation of the semi-analytical dipole-coupled model. We emphasize two key points. First, the dipole-coupled model closely matches the finite-element simulations in COMSOL Multiphysics, which capture the complete interaction but are much slower and computationally demanding due to their discretizing nature (for computational convenience, simulations use periodic boundary conditions, but the network and the domain are large enough that there are no artifacts from the periodicity). Second, the dipole-coupled

model can account for coupling that is not captured in the much simpler, analytic, treatment of non-coupled ribbons.

We analyze the response arising from the interaction between a small number of ribbons (two and three) in both planar and stratified configurations. To maintain generality, we assume that the ribbons are in a vacuum background and not on a particular substrate (the effects of a substrate can be accounted for through a modified Green function). The Fermi energies of ribbons are all set to 0.35 eV, with $\gamma = 3$ meV and $T = 300$ K.

Figure 2(a) shows the normalized absorption for the case of two elements of dissimilar size. We observe a correct prediction of a stronger resonance at 6.6 μm and a suppressed resonance at 6.3 μm. This contrasts with the inaccurate prediction from the non-interacting analysis (solid grey) which is inadequate for modeling the system. For the case of three dissimilar elements arranged in a planar configuration, figure 2(b) demonstrates a very good agreement between the dipole-coupled semi-analytical model (solid green) and the finite element simulations (dashed blue). The absorption response comprises the resonances from the three ribbons, but the interaction between the ribbons modulates the overall magnitudes, resulting in a noticeably weaker absorption of two narrower ribbons. Finally, the semi-analytical model also works for non-planar arrangements. Figure 2(c) depicts an example of a stratified three-ribbon configuration. For this configuration, the Green function is modified to account for the vertical coupling between the ribbons. Unlike the two previous planar cases, we observe the strongest absorption at the wavelength corresponding to the resonance of the ribbon with the intermediate width (55 nm), with the other two absorption peaks suppressed.

In all cases in figure 2, we see a very good match between the semi-analytical model and the finite-element simulations. The frequencies, linewidths, and relative strengths of the absorption peaks are predicted with good accuracy, with the semi-analytical model showing a slight blue-shift (e.g. $\Delta\lambda/\lambda \sim 0.004$ for the 6.6 μm peak in figure 2(a). In contrast, the non-interacting analysis that ignores the coupling between the elements models the system response poorly.

3. Results

Having established the coupled elements as building-blocks for the network, we proceed to show how the network can be designed to mimic a complex spectrum. As an illustration of a complex spectral profile, we select a target that resembles the absorption of NO. Figure 3 shows the low resolution NO absorption directly obtained from the NIST Chemistry WebBook [43]. The NO absorption profile contains multiple broad and narrow spectral features in the 5–8 μm range, rendering it a suitable target for exploring the potential of our approach.

The design of the mimicking network involves determining the optimal network geometry (i.e. ribbon widths and arrangements) and the optimal input signals (i.e. gate-tunable ribbon Fermi levels). Mathematically, we seek to maximize spectral matching over a bandwidth $\Delta\lambda$, which we quantify by a fidelity metric

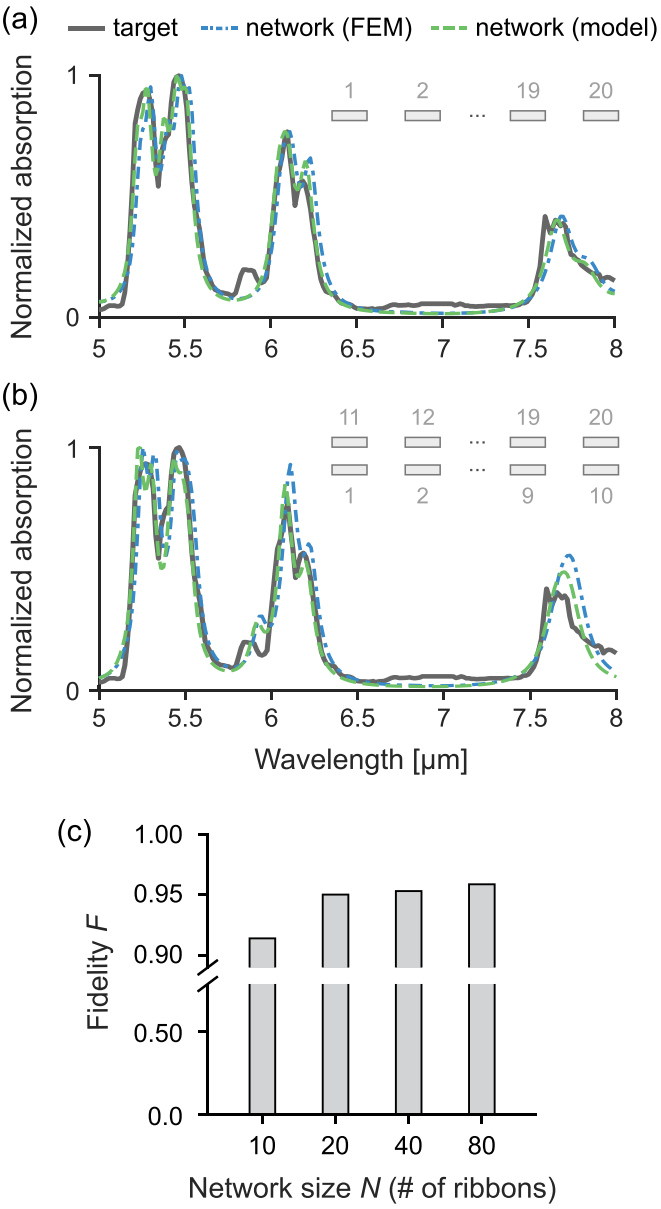

Figure 3. Spectrally mimicking a single complex target. The network is optimized to mimic the absorption profile of nitric oxide gas (NO) in a planar (a) and a stratified configuration (b). The model (dashed green), the target spectrum (solid purple), and the finite-element validation (dash-dotted blue) show good agreement. (c) Fidelity of matching (equation (10)) as a function of the network size.

$$F = 1 - \sqrt{\frac{1}{\Delta\lambda}\int_{\lambda_{\min}}^{\lambda_{\max}} \left[A_{\text{target}}(\lambda) - A_{\text{network}}(\lambda; \mathbf{W}, \mathbf{E}_{\text{F}})\right]^2 \mathrm{d}\lambda}. \tag{10}$$

This metric is a function of input vectors or ribbon widths $\mathbf{W} = [W_1, \ldots, W_N]$, and energies $\mathbf{E}_\mathrm{F} = [E_{\mathrm{F}1}, \ldots, E_{\mathrm{F}N}]$ within the network. Here, $\Delta\lambda$ denotes the bandwidth of the target absorption spectrum $A_\mathrm{target}(\lambda)$ and $A_\mathrm{network}(\lambda)$ denotes the spectrum of the network. Both spectra are scaled and normalized to unity, similar to outputs observed in spectroscopic measurements. The fidelity function, F, assesses the average spectral separation (or spectral overlap) between the target spectrum and the network spectrum. The limit of $F \to 1$ indicates a perfect overlap between the two normalized spectra.

Efficient maximization of fidelity F over the $N+N$ parameter space of ribbon widths and energies is made possible by the fact that gradients $\partial F/\partial W_i$ and $\partial F/\partial E_{\mathrm{F}i}$ can be computed very efficiently via auto-differentiation [44]. By combining gradient-based optimization (facilitated by auto-differentiation) with the speed of the semi-analytical model, we can explore a large design space of many ribbons and initial conditions. To mimic the NO spectrum, we start by generating a set of initial conditions for the vector $(\mathbf{W}, \mathbf{E}_\mathrm{F})$ using low-discrepancy Sobol sequences which help to achieve a well-distributed set of points within the $2N$-dimensional hypercube [45]. For each initial condition, the network is optimized using the method of moving asymptotes algorithm [46] (accessed through the NLopt package [47]). For all $E_{\mathrm{F}i}$ in the $\mathbf{E}_\mathrm{F}$ set, we impose Fermi energy bounds $0.1\,\mathrm{eV} \leqslant E_{\mathrm{F}i} \leqslant 0.5\,\mathrm{eV}$ and a minimum ribbon width of $40\,\mathrm{nm} \leqslant W_i$. We note that the combination of the highest E_F and the narrowest W_i sets a lower bound for the resonator wavelength ($\approx$4.3 μm). On the other hand, by making the ribbons wider and decreasing the Fermi level, scaling toward larger wavelengths is possible.

Figure 3(a) shows the optimized result for the network consisting of $N = 20$ ribbons (associated ribbon parameters are listed in B). We observe a very close match between the target spectrum (solid purple) and the network spectrum calculated using the dipole-coupled model (dashed green) and validated using a finite-element simulation (dotted blue). The fidelity of matching to the target spectrum is $F = 0.95$. Importantly, the network does not need to be in a single planar layer. Stratified, multi-layer, configurations can be beneficial to enhance the per-area response and minimize device size. Figure 3(b) demonstrates that the same optimization can be applied to a two-level configuration, yielding similarly very good performance ($F = 0.94$).

Figure 3(c) compares the achieved fidelity F for networks of varying sizes. For smaller networks ($N = 10$ and 20), a Sobol set of 1024 initial conditions is generated; for larger networks ($N = 40$ and 80), the results from smaller networks ($N = 20$ and 40, respectively) are used to inform pre-optimization initial conditions. Interestingly, even a smaller network of $N = 10$ elements can perform decently well ($F = 0.91$). Its spectrum is shown in Supplementary figure 1. The largest improvement is seen in the transition from an $N = 10$ to an $N = 20$ network ($F = 0.95$). Further enlarging the network continues to improve fidelity, but with diminishing benefits. This indicates that the intrinsic linewidth constraints become a limiting factor for spectral matching. We elaborate on this in section 4.

Finally, we explore how a single network of fixed geometry can mimic multiple different complex spectral profiles. We select spectral absorption profiles of NO, methane (CH_4), nitrogen dioxide (NO_2), nitrous oxide (N_2O) as targets (figure 4). For NO, the target spectrum is directly extracted from the database; for CH_4, N_2O, and NO_2, a spectral envelope is formed to mimic spectral trends, where the envelopes are created using spline interpolation over local maxima separated by at least 100 nm [43, 48]. Generally, for M targets, the design problem is to find one optimal network geometry ($\mathbf{W} = [W_1, \ldots, W_N]$) and M optimal Fermi energy sets ($\mathbf{E}_\mathrm{F}^{(k)} = [E_{\mathrm{F}1}^{(k)}, \ldots, E_{\mathrm{F}N}^{(k)}]$, for $k = 1, \ldots, M$) that, together, maximize the overall fidelity of spectral mimicking. Mathematically, we express the M-target fidelity function F_M as the average of the individual target fidelities:

$$F_M = \left\langle F^{(k)} \right\rangle_{k=1}^{M},$$
$$F^{(k)} = 1 - \sqrt{\frac{1}{\Delta\lambda^{(k)}} \int_{\lambda_\mathrm{min}^{(k)}}^{\lambda_\mathrm{max}^{(k)}} \left[A_\mathrm{target}^{(k)}(\lambda) - A_\mathrm{network}\left(\lambda; \mathbf{W}, \mathbf{E}_\mathrm{F}^{(k)}\right) \right]^2 \mathrm{d}\lambda}, \tag{11}$$

where $\langle \cdot \rangle_{k=1}^{M}$ denoting the average over M distinct targets. For a network of N elements (e.g. ribbons) seeking to mimic M targets, the dimension of the optimization space is $N + M \times N = (M+1)N$. This is equivalent to stating that we are looking for a single *fixed* network geometry described by N parameters (i.e. ribbon widths W_i) that under $M \times N$ *tunable* input signals (i.e. Fermi energies $E_{\mathrm{F}i}^{(k)}$) would optimally replicate M spectral profiles. The 'fixed' label refers to the fact that the geometry of the network is fixed at fabrication, whereas the electrical input signals remain tunable. As before, the auto-differentiable implementation makes it possible to calculate all gradients with respect to both input signals $\partial F_M/\partial E_{\mathrm{F}i}^{(k)}$ and the geometry $\partial F_M/\partial W_i$ very efficiently.

Figure 4 shows the four spectra of the network designed to replicate the four example gases. The network consists of $N = 20$ ribbons, in a planar arrangement, with the initial optimization parameters informed by results from figure 3. We observe a relatively high net fidelity value of $F_M = 0.91$. The spectra of NO and CH_4 show a better match ($F^\mathrm{NO} = 0.95$ and $F^{\mathrm{CH_4}} = 0.96$) relative to the spectra of NO_2 and N_2O ($F^{\mathrm{NO_2}} = 0.87$ and $F^{\mathrm{N_2O}} = 0.86$). This is attributed to the presence of narrower features in NO_2/N_2O spectra whose linewidths become too small for the network of this size and intrinsic graphene properties to accurately resolve. The optimized parameters of the network, the geometry and the four sets of input signals, are given in table B3 (which is of size $(M+1)N$, with $N = 20$ and $M = 4$). Overall, this example network showcases the promising potential of the coupled system to synthesize (and reconfigure between) complex spectral profiles.

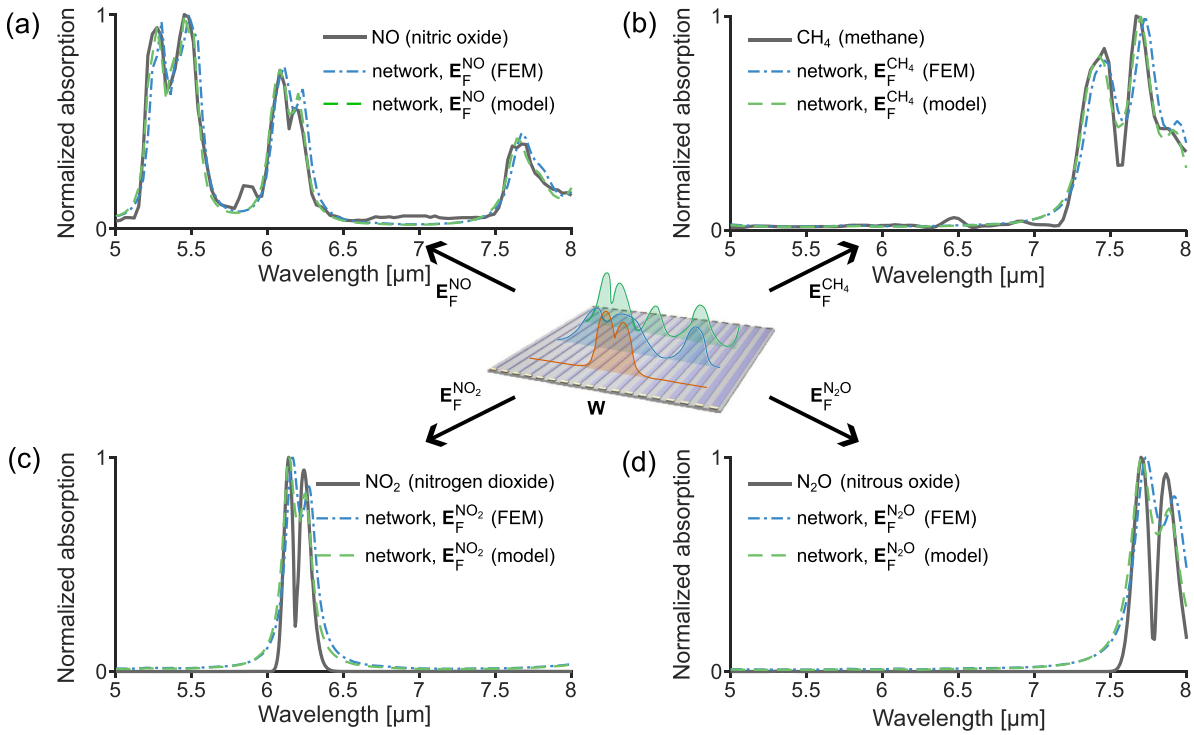

Figure 4. A single network reconfigures between four complex absorption profiles. To mimic the $M = 4$ target spectral profiles, we design a single optimal geometric arrangement and M optimal voltage inputs. A 4-target mean fidelity of $F = 0.91$ is achieved. The lines correspond to the model prediction (dashed green), target spectra (solid purple), and the finite-element simulation (dash-dotted blue).

4. Discussion and conclusion

We envision several relevant extensions of this work. In our analysis, we focused on graphene elements in a vacuum background to maintain generality. In a practical implementation, the effects of a substrate can be taken into account through a modified Green function. The introduction of a substrate, especially a nano-patterned or layered substrate, provides an additional opportunity to create more complex resonances (e.g. Fano resonances) and improve matching fidelity. Further, we note that the intrinsic material properties of graphene (e.g. damping γ) constrains the minimal linewidth of the spectral response and that higher carrier mobility would allow mimicking narrower resonances. The model can be generalized beyond dipole-coupling which might be relevant for ribbons with very small gaps between them. We have here analyzed networks in both planar and stratified configurations; in a practical device, one would want to consider the trade-off between the network density and the complexity of the gating architecture. Our results show that high fidelity of matching (>0.9) can be achieved in networks with $N \sim 20$ elements and the corresponding inputs; in practice, gating architectures have been demonstrated for significantly more input ports (e.g. $N = 96$ individually addressable elements in [49]), and graphene structures have been fabricated in stratified configurations [50].

In summary, we have theoretically demonstrated how a metamaterial network comprising coupled, gate-tunable, 2D-material resonators in graphene can mimic and reconfigure between multiple absorption spectra. By deriving a semi-analytical dipole-coupled network model and implementing it through auto-differentiation, we enabled a scalable design of high-dimensional networks with many elements and input signals. Our investigation shows that such networks can be designed to accurately match multiple complex spectral profiles, such as those resembling gases. Among known 2D materials, graphene has the strongest material-specific optical response in the longwave-IR/thermal-IR, independent of shape or structuring [51]. However, our proposed approach is general and could be applied to other tunable coupled-resonator structures and materials (e.g. resonators in solid state phase-change GeSbTe nanostructures [52] could extend the spectral mimicking functionality down to near-infrared/visible wavelengths). The underlying concept could facilitate the design of optical materials and platforms with excellent reconfigurability with applications in multi-spectral systems.

Data availability statement

All data that support the findings of this study are included within the article (and any supplementary files).

Acknowledgments

This material is based upon research supported by the Office of Naval Research under Award Number N00014-23-1-2627. This work was supported partially by the National Science Foundation through the University of Minnesota MRSEC under Award Number DMR-2011401. T C acknowledges the support of a research Grant (Project No. 42106) from Villum Fonden.

Appendix A. Elements of green function matrix

We derive equation (8) starting from the definition of the y-integrated xx-component of the free-space Green function (embedded in a medium of permittivity ε_{B}). The starting point is the nonretarded, uniform-medium Green tensor $\overleftrightarrow{\mathbf{G}}(\mathbf{r},\mathbf{r}') = \overleftrightarrow{\mathbf{G}}(\tilde{\mathbf{r}}) = \left[\hat{\tilde{\mathbf{r}}}\otimes\hat{\tilde{\mathbf{r}}} - \overleftrightarrow{\mathbf{1}}\right]/(4\pi k_{\mathrm{B}}^2|\tilde{\mathbf{r}}|^3)$ where $\tilde{\mathbf{r}} \equiv \mathbf{r}-\mathbf{r}'$. Taking the xx-component and integrating out the invariant y-direction, we obtain the induced field at $\mathbf{r}_\perp = (x,z)$ from a y-extended dipole 'line' at fixed $\mathbf{r}'_\perp = (x',z')$:

$$\begin{aligned} G(\mathbf{r}_\perp,\mathbf{r}'_\perp) &= G(\tilde{\mathbf{r}}_\perp) \\ &\equiv \int_{-\infty}^{\infty} G_{xx}(\tilde{\mathbf{r}})\,\mathrm{d}\tilde{y} \\ &= \frac{1}{4\pi k_{\mathrm{B}}^2}\int_{-\infty}^{\infty}\frac{3\tilde{x}^2}{|\tilde{\mathbf{r}}|^5} - \frac{1}{|\tilde{\mathbf{r}}|^3}\,\mathrm{d}y \\ &= \frac{1}{2\pi k_{\mathrm{B}}^2}\left(\frac{2\tilde{x}^2}{|\tilde{\mathbf{r}}_\perp|^4} - \frac{1}{\tilde{\mathbf{r}}_\perp^2}\right). \end{aligned} \tag{A.1}$$

Next, to obtain equation (8), we average equation (A.1) over the extent of a ribbon at i while setting $\mathbf{r}'_\perp = \mathbf{r}_{\perp j}$:

$$\begin{aligned} \bar{G}_{ij} &= \frac{1}{W_i}\int_i G(\mathbf{r}_\perp,\mathbf{r}'_\perp)\,\mathrm{d}x \\ &= \frac{1}{2\pi k_{\mathrm{B}}^2}\frac{1}{W_i}\int_i\left(\frac{2\tilde{x}^2}{|\tilde{\mathbf{r}}_\perp|^4} - \frac{1}{\tilde{\mathbf{r}}_\perp^2}\right)\mathrm{d}x \\ &= \frac{1}{2\pi k_{\mathrm{B}}^2}\frac{1}{W_i}\int_{-W_i/2}^{W_i/2}\left(\frac{2(\tilde{x}+x_{ij})^2}{\left[\sqrt{(\tilde{x}+x_{ij})^2+z_{ij}^2}\right]^4}\right. \\ &\quad \left. - \frac{1}{\left[\sqrt{(\tilde{x}+x_{ij})^2+z_{ij}^2}\right]^2}\right)\mathrm{d}\tilde{x} \\ &= \frac{2}{\pi k_{\mathrm{B}}^2}\frac{4(x_{ij}^2-z_{ij}^2)-W_i^2}{\left[(W_i+2x_{ij})^2+4z_{ij}^2\right]\left[(W_i-2x_{ij})^2+4z_{ij}^2\right]}. \end{aligned} \tag{A.2}$$

Table B1. Network parameters for figure 3(a). Center-to-center distances between ribbons are set to 120 nm.

i	W_i [nm]	E_i [eV]
1	44.2	0.151
2	40.2	0.187
3	52.7	0.357
4	56.3	0.100
5	57.4	0.100
6	50.0	0.420
7	50.4	0.121
8	54.8	0.482
9	53.5	0.211
10	50.4	0.333
11	55.7	0.499
12	59.0	0.125
13	60.0	0.105
14	47.3	0.331
15	50.6	0.140
16	52.2	0.427
17	57.4	0.124
18	41.3	0.442
19	48.6	0.420
20	56.7	0.250

Table B2. Network parameters for figure 3(b). Center-to-center distances between ribbons are set to 120 nm, and separation between two layers is set to 80 nm.

i	W_i [nm]	E_i [eV]
1	50.4	0.138
2	41.3	0.101
3	54.1	0.166
4	51.1	0.449
5	44.4	0.105
6	51.9	0.427
7	50.2	0.350
8	53.3	0.377
9	47.3	0.219
10	56.2	0.467
11	50.4	0.333
12	45.8	0.211
13	46.4	0.390
14	43.1	0.170
15	44.8	0.109
16	41.9	0.392
17	50.3	0.462
18	54.8	0.201
19	41.2	0.100
20	41.6	0.196

Appendix B. Network parameters

We tabulate the network parameters used for figures 3 and 4 of the main text in supplementary tables B1–B3.

Table B3. Network parameters for figure 4. Center-to-center distances between ribbons are set to 120 nm.

i	W_i [nm]	E_i^{NO} [eV]	$E_i^{CH_4}$ [eV]	$E_i^{N_2O}$ [eV]	$E_i^{NO_2}$ [eV]
1	44.1	0.151	0.491	0.145	0.110
2	40.3	0.189	0.120	0.143	0.160
3	52.7	0.357	0.235	0.147	0.352
4	56.2	0.105	0.050	0.144	0.168
5	57.5	0.103	0.176	0.254	0.209
6	50.0	0.420	0.142	0.230	0.190
7	50.4	0.118	0.097	0.135	0.195
8	54.8	0.482	0.260	0.233	0.352
9	53.4	0.217	0.064	0.236	0.127
10	49.8	0.330	0.050	0.123	0.108
11	55.8	0.500	0.247	0.245	0.370
12	58.9	0.119	0.277	0.126	0.187
13	60.0	0.105	0.186	0.170	0.123
14	46.9	0.330	0.215	0.147	0.175
15	50.6	0.141	0.245	0.173	0.108
16	52.2	0.427	0.149	0.148	0.350
17	57.5	0.125	0.237	0.101	0.145
18	41.0	0.456	0.121	0.099	0.171
19	48.5	0.420	0.238	0.140	0.318
20	56.9	0.252	0.268	0.248	0.119

ORCID iD

Ognjen Ilic https://orcid.org/0000-0001-8651-7438

References

[1] Chen H-T, Taylor A J and Yu N 2016 A review of metasurfaces: physics and applications *Rep. Prog. Phys.* **79** 076401

[2] Urbas A M *et al* 2016 Roadmap on optical metamaterials *J. Opt.* **18** 093005

[3] Khorasaninejad M and Capasso F 2017 Metalenses: versatile multifunctional photonic components *Science* **358** eaam8100

[4] Quevedo-Teruel O *et al* 2019 Roadmap on metasurfaces *J. Opt.* **21** 073002

[5] Ren M, Cai W and Xu J 2020 Tailorable dynamics in nonlinear optical metasurfaces *Adv. Mater.* **32** e1806317

[6] He S, Wang R and Luo H 2022 Computing metasurfaces for all-optical image processing: a brief review *Nanophotonics* **11** 1083–108

[7] Shaltout A M, Shalaev V M and Brongersma M L 2019 Spatiotemporal light control with active metasurfaces *Science* **364** eaat3100

[8] Abdollahramezani S, Hemmatyar O, Taghinejad H, Krasnok A, Kiarashinejad Y, Zandehshahvar M, Alù A and Adibi A 2020 Tunable nanophotonics enabled by chalcogenide phase-change materials *Nanophotonics* **9** 1189–241

[9] Shalaginov M Y *et al* 2020 Design for quality: reconfigurable flat optics based on active metasurfaces *Nanophotonics* **9** 3505–34

[10] Badloe T, Lee J, Seong J and Rho J 2021 Tunable metasurfaces: the path to fully active nanophotonics *Adv. Photon. Res.* **2** 2000205

[11] Malek S C, Overvig A C, Shrestha S and Yu N 2021 Active nonlocal metasurfaces *Nanophotonics* **10** 655–65

[12] Morsy A M and Povinelli M L 2021 Coupled metamaterial optical resonators for infrared emissivity spectrum modulation *Opt. Express* **29** 5840–7

[13] Zhu H, Li Q, Tao C, Hong Y, Xu Z, Shen W, Kaur S, Ghosh P and Qiu M 2021 Multispectral camouflage for infrared, visible, lasers and microwave with radiative cooling *Nat. Commun.* **12** 1805

[14] Tong J K, Huang X, Boriskina S V, Loomis J, Xu Y and Chen G 2015 Infrared-transparent visible-opaque fabrics for wearable personal thermal management *ACS Photon.* **2** 769–78

[15] Liu X and Padilla W J 2017 Reconfigurable room temperature metamaterial infrared emitter *Optica* **4** 430

[16] Arbabi E, Arbabi A, Kamali S M, Horie Y, Faraji-Dana M and Faraon A 2018 MEMS-tunable dielectric metasurface lens *Nat. Commun.* **9** 812

[17] She A, Zhang S, Shian S, Clarke D R and Capasso F 2018 Adaptive metalenses with simultaneous electrical control of focal length, astigmatism and shift *Sci. Adv.* **4** eaa9957

[18] Sherrott M C, Hon P W C, Fountaine K T, Garcia J C, Ponti S M, Brar V W, Sweatlock L A and Atwater H A 2017 Experimental demonstration of $>230^\circ$ phase modulation in gate-tunable graphene-gold reconfigurable mid-infrared metasurfaces *Nano Lett.* **17** 3027–34

[19] Ding L, Luo X, Cheng L, Thway M, Song J, Jin Chua S, Chia E E M and Teng J 2018 Electrically and thermally tunable smooth silicon metasurfaces for broadband terahertz antireflection *Adv. Opt. Mater.* **6** 1800928

[20] Di Martino G, Tappertzhofen S, Hofmann S and Baumberg J 2016 Nanoscale plasmon-enhanced spectroscopy in memristive switches *Small* **12** 1334–41

[21] Zanotto S, Blancato A, Buchheit A, Muñoz-Castro M, Wiemhöfer H-D, Morichetti F and Melloni A 2017 Metasurface reconfiguration through lithium-ion intercalation in a transition metal oxide *Adv. Opt. Mater.* **5** 1600732

[22] Wang Q, Rogers E T F, Gholipour B, Wang C-M, Yuan G, Teng J and Zheludev N I 2015 Optically reconfigurable metasurfaces and photonic devices based on phase change materials *Nat. Photon.* **10** 60–65

[23] Rensberg J *et al* 2016 Active optical metasurfaces based on defect-engineered phase-transition materials *Nano Lett.* **16** 1050–5
[24] Coppens Z J and Valentine J G 2017 Spatial and temporal modulation of thermal emission *Adv. Mater.* **29** 1701275
[25] Fang Z, Zheng J, Saxena A, Whitehead J, Chen Y and Majumdar A 2021 Non-volatile reconfigurable integrated photonics enabled by broadband low-loss phase change material *Adv. Opt.* **9** 2002049
[26] Wu S-H, Chen M, Barako M T, Jankovic V, Hon P W C, Sweatlock L A and Povinelli M L 2017 Thermal homeostasis using microstructured phase-change materials *Optica* **4** 1390
[27] Zhang Y *et al* 2021 Electrically reconfigurable non-volatile metasurface using low-loss optical phase-change material *Nat. Nanotechnol.* **16** 661–6
[28] Brar V W, Sherrott M C, Jang M S, Kim S, Kim L, Choi M, Sweatlock L A and Atwater H A 2015 Electronic modulation of infrared radiation in graphene plasmonic resonators *Nat. Commun.* **6** 7032
[29] Khaliji K, Biswas S R, Hu H, Yang X, Dai Q, Oh S-H, Avouris P and Low T 2020 Plasmonic gas sensing with graphene nanoribbons *Phys. Rev. Appl.* **13** 1
[30] Ilic O, Thomas N H, Christensen T, Sherrott M C, Soljačić M, Minnich A J, Miller O D and Atwater H A 2018 Active radiative thermal switching with graphene plasmon resonators *ACS Nano* **12** 2474–81
[31] Nagpal A, Zhou M, Ilic O, Yu Z and Atwater H 2023 Thermal metasurface with tunable narrowband absorption from a hybrid graphene/silicon photonic crystal resonance *Opt. Express* **31** 11227–38
[32] Alaee R, Farhat M, Rockstuhl C and Lederer F 2012 A perfect absorber made of a graphene micro-ribbon metamaterial *Opt. Express* **20** 28017–24
[33] Hajian H, Ghobadi A, Serebryannikov A E, Butun B, Vandenbosch G A E and Ozbay E 2019 VO_2-hBN-graphene-based bi-functional metamaterial for mid-infrared bi-tunable asymmetric transmission and nearly perfect resonant absorption *J. Opt. Soc. Am.* B **36** 1607
[34] Riso M, Cuevas M and Depine R A 2015 Tunable plasmonic enhancement of light scattering and absorption in graphene-coated subwavelength wires *J. Opt.* **17** 075001
[35] Velichko E A 2016 Evaluation of a graphene-covered dielectric microtube as a refractive-index sensor in the terahertz range *J. Opt.* **18** 035008
[36] Yao Y, Kats M A, Shankar R, Song Y, Kong J, Loncar M and Capasso F 2014 Wide wavelength tuning of optical antennas on graphene with nanosecond response time *Nano Lett.* **14** 214–9
[37] Li Q, Cong L, Singh R, Xu N, Cao W, Zhang X, Tian Z, Du L, Han J and Zhang W 2016 Monolayer graphene sensing enabled by the strong fano-resonant metasurface *Nanoscale* **8** 17278–84
[38] Han S, Kim S, Kim S, Low T, Brar V W and Jang M S 2020 Complete complex amplitude modulation with electronically tunable graphene plasmonic metamolecules *ACS Nano* **14** 1166–75
[39] de Abajo F J G and Manjavacas A 2015 Plasmonics in atomically thin materials *Faraday Discuss.* **178** 87–107
[40] Christensen T 2017 From classical to quantum plasmonics in three and two dimensions *PhD Thesis* Technical University of Denmark
[41] Koppens F H L, Chang D E and de Abajo F J G 2011 Graphene plasmonics: a platform for strong light–matter interactions *Nano Lett.* **11** 3370–7
[42] Falkovsky L A and Varlamov A A 2007 Space-time dispersion of graphene conductivity *Eur. Phys. J.* B **56** 281–4
[43] Linstrom P J and Mallard W G 2001 The NIST chemistry webbook: a chemical data resource on the internet *J. Chem. Eng. Data* **46** 1059–63
[44] Innes M 2018 Don't unroll adjoint: differentiating SSA-form programs (arXiv:1810.07951)
[45] Joe S and Kuo F Y 2003 Remark on algorithm 659: implementing Sobol's quasirandom sequence generator *ACM Trans. Math. Softw.* **29** 49–57
[46] Svanberg K 2002 A class of globally convergent optimization methods based on conservative convex separable approximations *SIAM J. Optim.* **12** 555–73
[47] Johnson. S G 2011 The NLopt nonlinear-optimization package (available at: http://github.com/stevengj/nlopt)
[48] Gordon I E *et al* 2017 The HITRAN2016 molecular spectroscopic database *J. Quant. Spectrosc. Radiat. Transfer* **203** 3–69
[49] Shirmanesh G K, Sokhoyan R, Wu P C and Atwater H A 2020 Electro-optically tunable multifunctional metasurfaces *ACS Nano* **14** 6912–20
[50] Gomez-Diaz J S, Moldovan C, Capdevila S, Romeu J, Bernard L S, Magrez A, Ionescu A M and Perruisseau-Carrier J 2015 Self-biased reconfigurable graphene stacks for terahertz plasmonics *Nat. Commun.* **6** 1–8
[51] Miller O D, Ilic O, Christensen T, Reid M T H, Atwater H A, Joannopoulos J D, Soljačić M and Johnson S G 2017 Limits to the optical response of graphene and two-dimensional materials *Nano Lett.* **17** 5408–15
[52] Hosseini P, Wright C D and Bhaskaran H 2014 An optoelectronic framework enabled by low-dimensional phase-change films *Nature* **511** 206–11